CHAPTER 14

Studying Kinesin Motors by Optical 3D-Nanometry in Gliding Motility Assays

Bert Nitzsche*, Volker Bormuth*, Corina Bräuer*, Jonathon Howard*, Leonid Ionov*, Jacob Kerssemakers†, Till Korten*, Cecile Leduc‡, Felix Ruhnow*, *and* Stefan Diez*

*Max Planck Institute of Molecular Cell Biology and Genetics, 01307 Dresden, Germany

†Kavli Institute of Nanoscience, Delft University of Technology, 2628 CJ Delft, The Netherlands

‡Centre de Physique Moleculaire Optique et Hertzienne, Université Bordeaux 1, CNRS (UMR 5798), 33405 Talence cedex, France

Abstract

Recent developments in optical microscopy and nanometer tracking have facilitated our understanding of microtubules and their associated proteins. Using fluorescence microscopy, dynamic interactions are now routinely observed *in vitro* on the

METHODS IN CELL BIOLOGY, VOL. 95

978-0-12-374815-7
DOI: 10.1016/S0091-679X(10)95014-0

level of single molecules, mainly using a geometry in which labeled motors move on surface-immobilized microtubules. Yet, we think that the historically older gliding geometry, in which motor proteins bound to a substrate surface drive the motion microtubules, offers some unique advantages. (1) Motility can be precisely followed by coupling multiple fluorophores and/or single bright labels to the surface of microtubules without disturbing the activity of the motor proteins. (2) The number of motor proteins involved in active transport can be determined by several strategies. (3) Multimotor studies can be performed over a wide range of motor densities. These advantages allow for studying cooperativity of processive as well as non-processive motors. Moreover, the gliding geometry has proven to be most promising for nanotechnological applications of motor proteins operating in synthetic environments. In this chapter we review recent methods related to gliding motility assays in conjunction with 3D-nanometry. In particular, we aim to provide practical advice on how to set up gliding assays, how to acquire high-precision data from microtubules and attached quantum dots, and how to analyze data by 3D-nanometer tracking.

I. Introduction

Optically following the live action of motor proteins at work has been a long-standing goal of biologists. However, observing the motors directly using light microscopy is technically much more challenging than imaging the huge polymeric filaments of the cytoskeleton along which the motors move. Even the narrow, 6-nm wide actin filaments can be imaged by dark-field (Nagashima and Asakura, 1980) or epi-fluorescence (Yanagida *et al.*, 1984) microscopy. Historically, this facilitated the development of the so-called "upside-down" motility assays early on. In these "gliding" assays, the motors are bound to a planar substrate (usually a glass coverslip), and the movement of the filaments across the surface (Fig. 1) is followed by time-resolved microscopy (Kron and Spudich, 1986). By reducing the motor density on the surface, gliding assays even provide the possibility to obtain recordings from individual motor proteins (Howard *et al.*, 1989). Yet, it has always been an attractive idea to visualize the movement of the motors rather than that of the filaments. In order to do so "stepping" motility assays, in which the filaments are bound to the substrate and the motor movement along the immobilized filaments is imaged, have been developed. This was first done by binding the motors to large, micron-sized beads, which could be followed by video microscopy (Sheetz and Spudich, 1983; Spudich *et al.*, 1985; Yanagida *et al.*, 1984) or held in an optical trap (Rief *et al.*, 2000; Schnitzer *et al.*, 2000; Svoboda *et al.*, 1993). Later on, Funatsu *et al.* pushed the sensitivity of the fluorescence microscope to the limit of being able to visualize individual motor molecules labeled with the cyanine-based fluorophores (Funatsu *et al.*, 1995). Using total internal reflection fluorescence (TIRF) microscopy, the processive movement of individual kinesin-1 molecules along microtubules was visualized by labeling the motors with Cy3 (Vale *et al.*, 1996) or with the green fluorescent protein (GFP) (Pierce *et al.*, 1997). Since then, the number of single-molecule fluorescence measurements of kinesin and dynein motors interacting with microtubules has vastly expanded. Nowadays, not only the stepping of motors is observed in these assays, but also diffusion and (de)polymerizing activities of motors

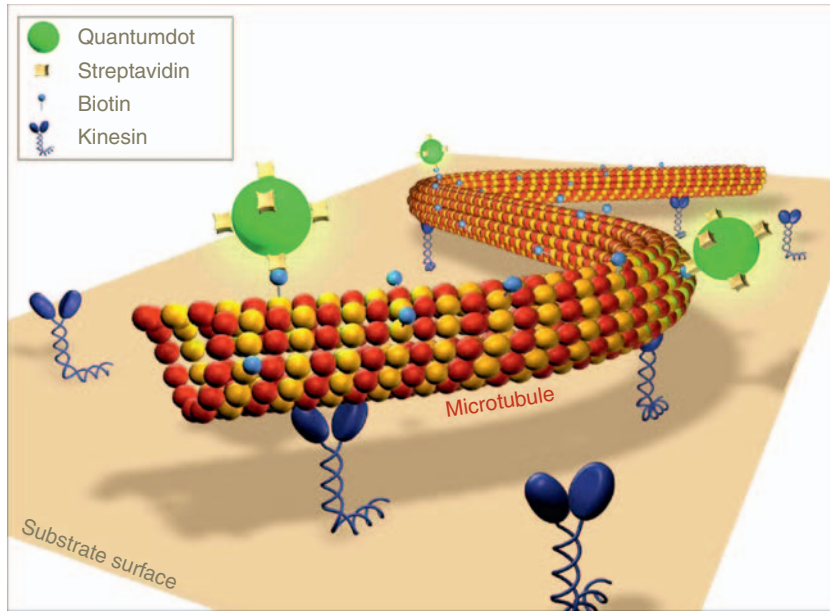

Fig. 1 Schematic diagram of a gliding motility assay in which reconstituted microtubules, tagged with semiconductor nanocrystals (quantum dots), are propelled over a kinesin-coated substrate surface. (See Plate no. 16 in the Color Plate Section.)

(and other microtubule-associated proteins) (Bieling *et al.*, 2007; Brouhard *et al.*, 2008; Fink *et al.*, 2009; Helenius *et al.*, 2006; Varga *et al.*, 2006, 2009).

Despite all the recent developments and groundbreaking results obtained in stepping motility assays, we think that there are still a number of compelling reasons to revisit the historically older gliding motility assays: (1) Fluorescently labeled filaments are bright objects that can be tracked with high precision. (2) Photostable optical reporters, such as quantum dots (QDs), can easily be attached to the filaments without interfering with the operation of individual motors. (3) Several strategies to determine the number of motors involved in transport are feasible. (4) The collective behavior involving multiple processive or nonprocessive motors can be studied over a wide range of motor densities. We will report methods and protocols that allow for experiments taking advantage of these benefits.

II. Setup of Gliding Motility Assays

When performing gliding motility assays, it is an essential prerequisite to immobilize the motor proteins on the surface in such a way that they lose as little activity as possible compared to a situation where they are free in solution or even to the *in vivo* situation. In particular, it is important to minimize the number of motors that only function partially, i.e., to avoid the existence of motors that bind rigorously to the filaments, unable to undergo their actual mechanochemical cycle. Along these lines, we regard the treatment of the surfaces and the method of motor

immobilization as the most critical steps in setting up a gliding motility assay. Unfortunately, there is no general protocol that works reliably with all types of motor proteins. Yet, there are certain concepts that, when adapted by some minor, but crucial, modifications, function with many different motor proteins. In the end, every gliding motility assay has to be optimized for the exact motor protein used, and evidence that the assay works is only provided by the facts that (1) the experiments are reproducible and (2) the gliding velocities are consistent with *in vivo* activity of the motor. Below we will list a number of example procedures and general hints on how to establish a "successful" gliding motility assay.

A. Surface Treatment and Flow-Chamber Preparation

Depending on the specific experiment, we routinely treat glass coverslips or silicon wafers with various cleaning and coating procedures to adjust the surface properties. The treated glass coverslips (for epi-fluorescence and TIRF measurements) or silicon wafers [for fluorescence-interference contrast (FLIC) measurements] then provide the surface of the flow chambers where the gliding motility experiments are performed in. Generally, surface preparation should be performed very carefully in a clean and dust-free environment to guarantee the reproducibility and the high quality of the experimental results.

Here we describe a simple, but effective, cleaning procedure (easy-clean), a method to passivate surfaces to prevent protein adsorption [based on polyethylene glycol (PEG)], a method to render surfaces highly hydrophobic (based on dichlorodimethylsilane), and an approach to generate surfaces, which gradually [in one dimension (1D)] change their capacity to bind proteins.

1. Easy-Clean Procedure

Load the glass coverslips or silicon wafer chips into porcelain or polytetrafluoroethylene (PTFE) racks. Place the racks into a glass container and fill with mucasol (1:20 dilution in deionized water) such that all coverslips/chips are completely covered. Sonicate (using Bransonic 2510, Branson, Danbury, CT, USA) for 15 min and rinse with deionized water for 2 min. Remove the water from the container using a (e.g., 1 ml) pipette tip connected to the vacuum line. Fill the container with ethanol, again immersing the coverslips/chips completely, sonicate for 10 min, and rinse with nanopure water for 2 min in the container. Take the racks out of the container and carefully blow dry the coverlips/chips using nitrogen.

When used under the microscope, these surfaces are mildly hydrophilic. Being usually devoid of any fluorescent particles, they are even suited for single-molecule fluorescence measurements.

Tip: We store the coverslips/chips (prepared by the easy-clean procedure as well as by the methods listed below) in a dry container, which is sealed such that no dust can get onto the surfaces.

2. Protein-Repelling Surfaces (Based on PEG-Silane)

To passivate surfaces, we use a procedure adapted from Papra *et al.* (2001) as follows: Load the glass coverslips or silicon wafer chips into porcelain or PTFE

racks. Place the racks into a glass container and fill with an ethanol/water mix (1:1). Sonicate for 5 min and rinse with deionized water for 2 min. Expose the coverslips to piranha-cleaning solution (60 ml sulfuric acid and 20 ml hydrogen peroxide; add the hydrogen peroxide last) for 10 min, rinse three times with nanopure water and sonicate in nanopure water for 10 min. After blow drying them using nitrogen, they are ready for the grafting of PEG. Incubate the coverslips/chips for 18 h at room temperature in 25 ml of toluene supplemented with 57.5 mg of 2-[methoxy (polyethyleneoxy)propyl]trimethoxysilane (PEG-silane, 90%) and 20 µl HCl (37%). Ensure constant stirring and cover the container. In a subsequent cleaning procedure, rinse the coverslips/chips once in toluene, twice in ethanol, twice in nanopure water, and sonicate in nanopure water for 2 min.

Proteins will be repelled from a pegylated surface. That is why a substrate treated this way is suitable as a counterpart to the "imaging surface" of a flow chamber. If the nonimaged surface is pegylated, then all proteins of interest will interact with the "imaging surface" only.

3. Hydrophobic Surfaces (Based on Dichlorodimethylsilane)

This procedure is described in Chapter 13 by Gell *et al.*, this volume. We use hydrophobic surfaces to strongly adsorb antibodies (as adapter proteins for specific motor molecules) in combination with the possibility to block the rest of these surfaces against nonspecific protein binding by casein or Pluronics (see below).

4. Gradient Surfaces (Based on PEG)

Clean the highly polished silicon wafer chips (final chip size 50×10 mm, {100} orientation) in an ultrasonic bath with chloroform for 30 min. Place them in piranha-cleaning solution (see above) for 1 h and rinse several times with nanopure water. Spin-coat a thin layer (thickness 1.5 nm) of polyglycidylmethacrylate (PGMA, $M_n = 50{,}000$ g/mol, 0.02% in chloroform [we found this to work even better than using methylethylketone as solvent as reported previously (Ionov *et al.*, 2005)] on the chips. Spin-coat a thin film (thickness about 200 nm) of PEG-NH_2 (2% solution in chloroform, PEG-NH_2, $M_n = 5000$ g/mol, $M_w = 5400$ g/mol) on top and let the sample anneal for 1 h on a stage with a 1D temperature gradient (40–90°C along a length of 50 mm). Upon this heating step, the grafted PEG layer will form due to the chemical reaction between the terminal amino groups of the PEG and the epoxy groups of the PGMA. The temperature gradient translates to a gradient in the grafting density caused by the temperature dependence of the grafting kinetics. Remove ungrafted polymer using Soxhlet extraction in chloroform for 3 h [see also Ionov *et al.* (2005) for more details].

Such surfaces, which gradually change their protein-repelling properties (based on the PEG gradient) in 1D, can be applied for combinatorial and high-throughput investigations of proteins. When motor proteins are bound to such surfaces, they allow for probing the interactions of filaments with motors of different density on one sample surface, as well as for the sorting of filaments according to their length (Ionov *et al.*, 2005).

5. Flow-Chamber Preparation

The general procedure we use to assemble our flow chambers is described in Chapter 13 by Gell *et al.*, this volume. Apart from double-sided Scotch tape to confine the flow channels, we also use Parafilm or Nescofilm as an alternative. Flow-chamber assembly is then as follows: Cut the Para-/Nescofilm in stripes using a (razor) blade or a laser cutter (Speedy 100C 25W, Trotec, Marchtrenk, Austria). Place the prepared Para-/Nescofilm stripes on top of a 22×22 mm coverslip and cut off (using a razor blade) those parts of the stripes that protrude over the edges of the coverslip. Place the top coverslip (18×18 mm or silicon chip) in a central location on the stripes and transfer the assembly (22×22 coverslip facing down) to a heating plate with a temperature of $\approx$120°C for Parafilm or $\approx$150°C for Nescofilm. The two coverslips (or coverslip/silicon chip) will be firmly joined by the melting Para-/Nescofilm. This process can be well monitored by a change in the optical properties of the Para-/Nescofilm. Gently applying a bit of pressure to the top coverslip/chip during the melting process ensures a tight sealing and eliminates air bubbles that might have formed above or beneath the stripes. Without delay, place the flow chamber onto the surface of a metal (e.g., aluminum) block for fast cooling. Mounting the assembly in the appropriate holder (see also Chapter 13 by Gell *et al.*, this volume) is the last step before the channels (volume approximately $3 \times 18 \times 0.1$ mm ≈ 5 µl) of the flow chamber can be filled with solutions.

Tip: When using a pegylated coverslip (with an extremely hydrophilic surface) as one side of the flow chamber, double-sided Scotch tape and parafilm stripes frequently lift-off the pegylated surface and hence the channels become leaky. We therefore recommend using Nescofilm in conjunction with pegylated surfaces.

Tip: When assembling the flow chambers, take care to not expose bare surfaces to dust. Apply the same caution as during the surface preparation.

B. Microtubule Preparation

For gliding motility assays, microtubules are commonly reconstituted from purified tubulin. Thereby, their physical structure, including the number of protofilaments and the stiffness, strongly depends on the assembly conditions (Meurer-Grob *et al.*, 2001; Pierson *et al.*, 1978; Ray *et al.*, 1993). Below, we will describe the generation of stable (i.e., nondynamic) microtubules using the slowly hydrolyzable GTP-analogue GMP-CPP with/without further stabilization using Taxol. In order to allow for the attachment of streptavidin-coated QDs as fluorescent markers, part of the tubulin used in the polymerization reaction is biotinylated.

1. Biotinylated GMP-CPP Microtubules

Supplement 100 µl BRB80 (80 mM PIPES/KOH pH 6.9, 1 mM $MgCl_2$, 1 mM EGTA) by 2 µM tubulin, 4 mM $MgCl_2$, and 1 mM GMP-CPP. Tubulin may be a mixture of 5–50% fluorescently labeled (e.g., Alexa 488 or TAMRA), 2–50% biotinylated, and 50–93% unlabeled tubulin. (Note: Because very high tubulin labeling ratios can lead to artifacts in the interaction of motor proteins with the filaments, we never use more than 50% labeled tubulin in the polymerization reaction) Allow the microtubules to assemble for ≥ 2 h at 37°C. Centrifuge the

microtubule solution at 100,000 × *g* for 5 min and resuspend in BRB80 (final tubulin concentrations 0.4–4 μM). For more details, see Nitzsche *et al.* (2008).

Tip: If the concentration of free tubulin is very low in the final solution (e.g., after centrifugation and dilution in high volumes), microtubules may depolymerize within a few hours. Performing the centrifugation step only shortly before using the microtubules greatly reduces this problem.

Tip: The stability of GMP-CPP microtubules can be quite variable due to residual GDP/GTP in the initial tubulin solution (Caplow *et al.*, 1994; Caplow and Shanks, 1996). The durability of the microtubules can be greatly improved by an additional cycling step when preparing the tubulin solution (see Chapter 13 by Gell *et al.*, this volume).

Tip: More than 95% of the microtubules assembled in the presence of GMP-CPP consist of 14 super-twisted protofilaments (Hyman *et al.*, 1995; Meurer-Grob *et al.*, 2001).

2. Biotinylated Double-Stabilized Microtubules

Prepare biotinylated microtubules using GMP-CPP (as described above). However, resuspending the microtubules after the centrifugation step, supplement the BRB80 with 10 μM Taxol and keep this amount of Taxol present in all subsequent solutions. Microtubules stabilized this way are stable for weeks at room temperature.

C. Surface Immobilization of Motor Proteins

We use two types of strategies to immobilize motor proteins on surfaces: nonspecific and specific binding. In the simplest case (nonspecific binding) motor proteins are allowed to adsorb to surfaces precoated with other "space filling" proteins (Howard *et al.*, 1993). This nonspecific approach works for some kinesin motors (e.g., kinesin-1). For other motor proteins, however, procedures targeting specific sequences of the motor proteins can significantly improve the quality of motility assays. Thereby, bioactive linker molecules (e.g., specific antibodies or streptavidin) that are directed toward specified regions distal to the motor domain (e.g., purification tags, GFP or biotinylated sites) are first attached to the surface. After the rest of the surface is blocked by other space filling proteins (or polymers), the motor molecules can bind to the surface in a directed manner (Crevenna *et al.*, 2008; Kerssemakers *et al.*, 2006; Leduc *et al.*, 2007). Below we describe the immobilization of kinesin-1 motors using (1) nonspecific binding to casein-coated surfaces and (2) specific binding using penta-His antibodies against a tag sequence added to the tail of the kinesin-1 heavy chain.

1. Nonspecific Immobilization

Construct a flow chamber, using easy-clean glass coverslips, as described above. Flow in 0.5 mg/ml casein in BRB80 into one of the channels and let the surfaces incubate for 5 min. Replace the solution by 100 μg/ml kinesin-1 in BRB80 supplemented with 10 μM to 1 mM ATP and 0.2 mg/ml casein and wait 5 min.

The actual gliding motility assay is then performed by perfusing a microtubule-containing "motility solution" [BRB80 augmented with microtubules, 10 μM to

1 mM ATP, 0.2 mg/ml casein, and an oxygen scavenger mix of 20 mM D-glucose, 0.02 mg/ml glucose oxidase, 0.008 mg/ml catalase, and 10 mM dithiothreitol (DTT) or 0.5% β-mercaptoethanol (BME)] into the flow chamber.

Tip: While casein has been reported to be a blocking agent which effectively prevents kinesin-1 from denaturing at the surface (Ozeki *et al.*, 2009), other proteins (e.g., BSA) may be more effective for other motors. However, even in cases where the surface blocking strategy is not based on casein, supplementing the ATP-containing motility solution with casein (≈0.2 mg/ml) often helps to achieve reliable motility.

Tip: Gradients in the density of motor proteins can be generated when motor proteins are nonspecifically adsorbed onto surfaces prepared with PEG gradients (see above).

2. Specific Immobilization (Via Antibodies)

Construct a flow chamber, using hydrophobic glass coverslips, as described above. Flow in penta-His antibodies in BRB80 (about 20 or 0.2 μg/ml for high or low kinesin concentration assays, respectively). Wait 5 min. Perfuse 0.5 mg/ml casein in BRB80 to prevent nonspecific protein binding. Wait 5 min. Flow in 10 μg/ml kinesin-1 (with a His-tag) in BRB80 supplemented with 0.2 mg/ml casein and 10 μM to 1 mM ATP. Incubate for 5 min to bind the motors specifically to the antibodies by their His-tags. Similar to the procedure described above, the actual gliding motility assay is then performed by perfusing a microtubule-containing "motility solution" into the flow chamber [see also Leduc *et al.* (2007)].

Tip: The procedure described above is also applicable for flow chambers with easy-cleaned (see Section II.A) surfaces.

Tip: Make sure your antibody solution does not contain any contaminations that might block the surface of your flow chamber, thereby preventing effective adsorption of the antibodies.

Tip: Alternative to casein, Pluronic F127 (or similar copolymers) can be used to prevent nonspecific protein binding to hydrophobic surfaces (Crevenna *et al.*, 2008; Kerssemakers *et al.*, 2006). Note that Pluronics are applicable for passivation of hydrophobic surfaces only.

Tip: For other motors, sandwich-like, antibody-binding assays, providing longer and more flexible linkage between surface and motor proteins, might prove useful. For example, biotinylated anti-GFP antibodies (bound to surface-immobilized neutravidin) can be used to specifically bind GFP-tagged kinesin-8 motor proteins (Varga *et al.*, 2009). Similarly, surface-immobilized protein A can be used to bind an intermediate layer of (nonbiotinylated) anti-GFP antibodies.

Tip: Additional methods to specifically bind His-tagged motor proteins to surfaces, e.g., by nitrilotriacetic acid (NTA)–functionalized Pluronic (deCastro *et al.*, 1999) or NTA–PEG (Bieling *et al.*, 2008), have been reported in the literature.

D. Attachment of Fluorescent Markers to Microtubules

In order to study motor behavior in gliding assays, microtubule movement on motor-coated surfaces has to be measured with nanometer precision. For this purpose, fluorescence microscopy combined with nanometer tracking is well suited.

First, microtubules can be labeled with a multitude of fluorescent dyes along their lattices, making the contours of the filaments visible. Second, well-separated subresolution fluorescent emitters (such as QDs) can be coupled to microtubules. A combination of both labeling approaches can be applied to observe rotations of microtubules around their longitudinal axes (Nitzsche *et al.*, 2008).

1. Fluorescent Dyes

Fluorescent microtubules are most commonly generated by polymerizing tubulin heterodimers, a fraction of which are labeled with fluorescent dyes. The choice of fluorophores depends on several factors, such as emission and absorption spectra (especially when doing multicolor imaging), brightness, photostability, and compatibility with microtubule polymerization (see Chapter 13 by Gell *et al.*, this volume for details). Chemical coupling of fluorescent dyes to tubulin is commonly performed using succinimidyl chemistry. The procedure we are using is similar to that of Hyman *et al.* (1991). Besides, tubulin labeled with different dyes or bioactive small molecules (such as biotin) is commercially available.

2. Quantum Dots

QDs are fluorescent semiconductor nanocrystals that exhibit a number of superior optical properties compared to fluorescent dyes (Giepmans *et al.*, 2006; Resch-Genger *et al.*, 2008): (1) they emit at sharply defined wavelengths (dependent on their geometrical size), (2) their excitation spectrum is very broad (ranging from the UV up to closely below the emission wavelength), (3) they are very bright (due to their high extinction coefficients and quantum yields), and (4) their superior photostability guarantees long life-times in fluorescence imaging. These features make QDs ideally suited for high-precision nanometer tracking, in particular in multicolor applications. One drawback of the QDs is that they blink on various timescales (ranging from submilliseconds to many seconds). Although there is no way to eliminate blinking completely, it has been reported that the use of the reducing agents BME and DTT reduces blinking dramatically (Hohng and Ha, 2004). There are also recent reports about the synthesis of nonblinking QDs (Chen *et al.*, 2008; Mahler *et al.*, 2008; Wang *et al.*, 2009), though they are not commercially available.

QDs are available in a wide range of emission wavelengths. When choosing the right QDs, we find two considerations important: (1) to avoid crosstalk with the signal of the labeled microtubules, and (2) to optimize the emission intensity. Note that QDs emitting in the longer wavelength range (i.e., in the red spectrum) exhibit significantly higher extinction coefficients than those emitting at lower wavelengths. Red QDs are therefore better suited for nanometer tracking applications, where localization uncertainty scales with the inverse of the square root of the number of detected photons (Thompson *et al.*, 2002).

Labeling of microtubules with QDs is performed in the flow chamber (see following example): Wait 5 min after perfusion of the microtubule-containing motility solution (see Section II.C), in order to let microtubules bind to the motor-coated surfaces. Incubate the flow chamber with motility solution which, however, contains 2–50 pM streptavidin-conjugated QD 655 instead of microtubules. Wait 5 min. Wash

out QDs using 60–100 µl of motility solution (without microtubules). At moderate labeling rates, i.e., when individual QDs are well separated in the optical microscope, there is no significant influence of the QDs on the gliding velocity of the microtubules.

Tip: When specifically immobilizing motors on the surface via antibodies, increased nonspecific binding of streptavidin-conjugated QDs to the surface might occur. In this case, try to keep the antibody concentration as low as possible. In particular, control the motor density on the surface via the antibody concentration rather than using high antibody concentrations in conjunction with variable motor concentrations.

Tip: According to the manufacturer's specifications, the casein we use may cause interference with the biotin–streptavidin system for it contains variable amounts of biotin. While we did not find this to be a critical issue in our assays, we precautionarily store the QDs in their original stock solution (as purchased) and add them to the respective solution just before use.

Tip: It is also possible to bind QDs to microtubules in the test tube (Leduc *et al.*, 2007). However, when doing so, be aware that elevated concentrations of microtubules and QDs, high biotinylation rates of the microtubules, and/or long incubation times may lead to microtubule–microtubule cross-linking. In addition, free biotinylated tubulin may bind to and even saturate the streptavidin on the QDs.

E. Imaging of Microtubule Motility

In our standard setup for epi-fluorescence imaging, we acquire time-resolved movies of microtubule motility using an inverted fluorescence microscope (Axiovert 200M, Zeiss, Oberkochen, Germany) with a variety of optical objectives (e.g., 100× oil 1.3 NA, 63× water 1.2 NA, 40× oil 1.3 NA, Zeiss) in combination with an EMCCD camera (Ixon DV 897, Andor, Belfast, UK). Fluorescence excitation is achieved using either a mixed gas argon–krypton laser (Innova 70C Spectra; Coherent, Santa Clara, CA, USA) or a liquid-waveguide-coupled Lumen 200 metal arc lamp (Prior Scientific Instruments Ltd., Cambridge, UK). Image acquisition and basic data processing is done using a MetaMorph software package (Universal Imaging, Downingtown, PA, USA) controls. In the following, we describe modifications enabling dual-color TIRF and FLIC microscopy as well as a method to control the temperature of the gliding assay.

1. Total Internal Reflection Fluorescence Microscopy

TIRF microscopy allows for high-contrast imaging of fluorescent objects within the evanescent field near transparent substrate surfaces. The setup we are using consists of a commercially available TIRF slider and an alpha Plan-Apochromat 100× oil 1.46 NA DIC objective (both Zeiss).

2. Fluorescence-Interference Contrast Microscopy

FLIC microscopy can be employed to obtain nanometer height information of fluorescent objects above reflective surfaces. Direct and indirect light exciting a fluorophore in the vicinity of a reflective surface will self-interfere (as will the direct and indirect emission light) leading to a periodic modulation of the detected intensity

as function of object height above the surface (the "FLIC curve") (Kerssemakers *et al.*, 2006; Lambacher and Fromherz, 1996). As a consequence of the interference, minimum intensity is observed directly on the reflecting surface while the first maximum is located about 100–150 nm above the surface. To apply FLIC microscopy to gliding motility assays, flow chambers have to be constructed such that the side toward the objective is transparent while the one distal to the objective is reflective—we use a glass coverslip and a silicon chip, respectively. The sample can be illuminated using a fluorescence lamp or a laser and imaging is performed "through" the flow chamber, using a water immersion objective, to minimize spherical aberrations. In order to acquire data in the sensitive range of the FLIC curve, i.e., in the range where the detected intensity varies strongly with distance above the surface, the silicon chips are featured with layers of transparent silicon oxide ranging in height from a few nm to about 80 nm. For an *in situ* calibration of the FLIC curve, silicon chips with varying heights of silicon oxide (Lambacher and Fromherz, 1996) or tilted microtubules can be used (Kerssemakers *et al.*, 2006) (see also Fig. 5 in Section III.C).

3. Dual-Color Imaging

For the simultaneous imaging of microtubules (e.g., labeled with green Alexa 488) and QDs (e.g., QD 655 emitting in the red at 655 nm), we use single-band excitation in the blue range of the spectrum of light. For detection, we separate the emission colors employing a spectral beam splitter (W-view A8509, Hamamatsu Photonics K. K., Hamamatsu City, Shizuoka Pref., Japan) mounted between the microscope and the camera. The exact specifications of the fluorescence filters in microscope and beam splitter will depend on the actual fluorophores and QDs used [see Nitzsche *et al.* (2008) for a specific example]. The signals of the two color-channels are then recorded on two different halves of the same CCD camera chip. In order to calibrate the dual-color overlay, we sparsely deposit multicolor tetraspeck fluorescent beads (0.2 µm diameter) onto the surface before the motor immobilization procedure. While an exact (hardware-based) alignment of the two color-channels is not possible due to perturbations in the optical paths, the multicolor beads can be used to generate a (software-based) offset map between the channels.

Tip: While laser illumination enables high excitation intensities within a narrow spectral band, it often comes with spatial inhomogeneities in the illumination over the field of view. These inhomogeneities result from the long coherence length of the laser light which causes unwanted interference effects in the imaging systems, mainly due to scattering. We therefore often perform our experiments using illumination by a metal arc-lamp, providing us with spatially homogeneous illumination yet at sufficient light intensity.

4. Temperature Control

To allow for highly reproducible measurements of gliding velocities, tightly controlling the temperature of the assays during imaging can be essential. The usual approach of heating the stage (and/or the objective) is rather slow and does not allow for cooling the sample. To overcome these drawbacks, we mount the flow chamber on a Peltier element connected to a heat sink. The Peltier element is powered by a remotely controllable, automated laboratory power supply (Elektro

Automatik EA-PS 3016-10B, Viersen, Germany). To change between heating and cooling, a computer-controlled polarity switch (constructed in-house) is employed for switching the polarity of the Peltier current. The temperature on the Peltier element is measured using a thermometer with analog readout capability (Physitemp BAT 10, Clifton, NJ, USA) and a tissue implantable thermocouple microprobe (Physitemp IT-23). Both the thermometer and the power supply are connected to the imaging computer via an analog I/O PCI card (DaqBoard/2000, IOtech, OH, USA-now Measurement Computing Corporation, Norton, MA, USA). Temperature control has been programmed in a journal within the imaging software (Metamorph, Universal Imaging Corp., Downington, PA, USA). Based on the temperature readout, the current necessary for the Peltier to reach the target temperature is calculated using the characteristic current–temperature relation of the Peltier element. However, if temperatures more than 10 K above or below room temperature are to be sustained for longer time periods, the power needs to be constantly adapted, to compensate for thermal power loss of the Peltier element. For this purpose an appropriate fine-tuning algorithm constantly checks whether the actual temperature is still within 0.2 K of the target temperature. If that is not the case and the temperature gradient is below 0.2 K/s, the algorithm adjusts the temperature the Peltier element is assumed to have at zero power (initially set to room temperature). That way, the temperature regulation is very robust not only against thermal power loss, but also against changes of ambient temperature and inaccuracies of the assumed characteristics of the Peltier element.

Our approach [for more details, see Korten (2009)] allows one to control the temperature of the sample in the range from –10 to 100°C with a response time of a few seconds. Like other methods, our setup shows defocusing upon temperature changes. However, the defocusing has turned out to be linear with temperature and is compensated for by adjusting the *z*-position of the microscope stage (motorized focus in the inverted Zeiss 200M) by 0.77 μm per 1 K temperature difference. While focus compensation is too slow for very fast temperature switches, the image is back in focus as soon as the temperature change slows down, making manual refocusing obsolete in most cases.

5. Practical Issues

1. Make sure the sample is tightly fixed on the microscope stage in order to avoid unwanted shifting in the field of view. If necessary, be creative to fix its position by additional means.
2. Thermal drift during imaging can be reduced significantly when allowing the flow chamber (including the sample holder) to thermally equilibrate for about 2 min before image acquisition (flow chamber already in contact with the immersion fluid, if nonair objectives are used).
3. Airflow in air-conditioned rooms can cause quite dramatic stage drift. A simple yet effective solution is to build a closed box (e.g., made of transparent polymethyl methacrylate) around the microscope.
4. To compensate for residual stage drift, bright fluorescent beads (e.g., tetraspeck beads) can be used as drift control in the sample. Ideally the signal of the beads should be much brighter than that of the fluorescent objects of interest. Otherwise, noise from bead tracking will significantly contribute to the localization error of the fluorescent objects of interest (see also Section III.B). If single beads are not

bright enough, the signal can be virtually improved by averaging the positions of multiple beads.

5. When imaging for a longer period of time, buffer will evaporate from the edges of the flow channels causing changes in buffer concentration and ionic strength. In order to avoid this, sealing the channel with vacuum grease or sigillum wax helps. If solutions within the flow chamber still need to be replaced during the experiment, an alternative is provided by placing some water-soaked cellulose towels beside the flow chamber and covering both with a small plastic box (like the lid of a pipette box).
6. Even without sophisticated microfluidic devices, solutions in flow channels can be exchanged keeping the sample in the very same field of view. The principle is that on the one side of the flow channel the desired solution is fed while the solution to be removed from the channel is sucked up with a piece of filter paper at the same time. With a steady hand and a bit of practice, this procedure works surprisingly well. When working carefully, the sample is only shifted by a few nanometers.
7. When exchanging solutions in the flow chamber during sample illumination, we sometimes observe a nonreversible slowdown of motility. We attribute this phenomenon to photo effects probably caused by oxygen which is introduced into the flow channels during buffer exchange. We avoid this problem by interrupting the illumination for the duration of the buffer exchange. Waiting for an additional 10–30 s seems to be sufficient time for the oxygen scavenger system to deplete the oxygen from solution.

III. Analysis of Microtubule and Quantum Dot Movements

Time-resolved image sequences of microtubules gliding on motor-coated surfaces contain valuable information about the activity of the motor proteins. In order to extract these data, a number of image-processing tools are available. We will describe the application of maximum intensity projections and kymographs as quick (and easy) evaluation methods to study motor trajectories and velocity. In order to resolve gliding parameters in the nanometer range (also allowing to search for stepwise motor movements), we use 2D tracking algorithms which involve sub-pixel fitting procedures. Moreover, we employ interference-based imaging methods to extend the nanometer tracking into the third dimension.

A. Quick Motility Evaluation in Two Dimensions

When aiming to quickly and efficiently determine a number of key motility parameters, such as the gliding velocities of microtubules, it is often sufficient to determine the position of the fluorescent objects with a precision in the order of the pixel size. Maximum intensity projections or kymographs—available in standard image acquisition and processing software packages such as ImageJ (public domain, Java-based project by Rasband, W., National Institutes of Health, USA, http://rsbweb.nih.gov/ij/) or Metamorph (Universal Imaging, Downingtown, PA, USA)—usually suffice for this purpose. While maximum projections can inherently provide data about multiple mobile objects within the field of view, they do not carry any

temporal information. Kymographs, on the other hand, are used to analyze the trajectories of single objects moving along a given path in a time-resolved manner.

1. Maximum Intensity Projections

Maximum (intensity) projections are images whose pixel values represent the maximum value of the respective pixel within a whole stack of images. For stacks of sequentially acquired images from the same field of view, a maximum projection therefore depicts the trajectories of the moving objects. Based upon this, the fastest way to obtain the velocities of gliding microtubules (Fig. 2A and D) is to measure their distances traveled in a maximum projection and divide this value by the time that passed between the acquisition of the first and last image in the stack. If the signal of a point source of light (like a microtubule-attached QD) is available, this can be directly used to measure the distance traveled by a microtubule (provided the QD is firmly attached to the microtubule ensuring there is no shift with respect to each other). If the whole microtubule is labeled by fluorescent dyes, a maximum projection will display the path of the microtubule plus its length. To then determine the velocity values correctly, the initial and final positions of either the leading or the trailing microtubule tip have to be visualized in the maximum projection. A very convenient way of doing so is a three-color overlay of (1) the first frame of the stack,

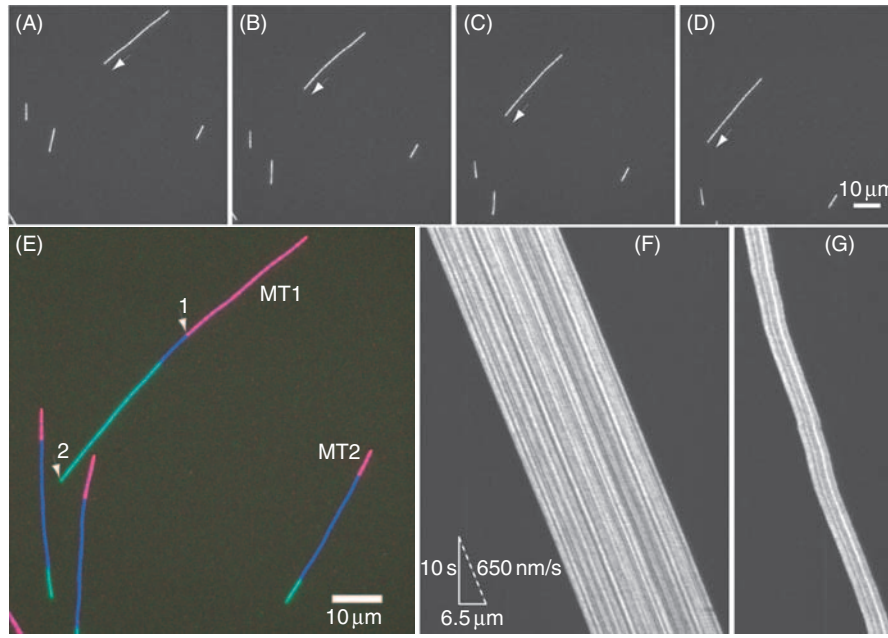

Fig. 2 Quick motility evaluation in two dimensions. (A–D) Fluorescence images of motile microtubules at 0 s (A), 20 s (B), 40 s (C), and 60 s (D). The arrows indicate the leading tip of one microtubule. Images are a subset from a continuously acquired movie (streaming mode over 60 s) with 10 frames per second. (E) Three-color overlay of first frame of the movie (red), last frame of the movie (green), and maximum projection of the path in between (blue). The distance traveled by the microtubule is measured between arrow 1 and 2. (F, G) Kymographs for microtubules MT1 moving with uniform velocity (F) and MT2 moving with nonuniform velocity (G). (See Plate no. 17 in the Color Plate Section.)

(2) the last frame of the stack, and (3) the maximum projection depicting the path in between (see Fig. 2E).

There are three major restrictions to maximum projections: (1) If a stack is very long or contains many moving objects, maximum projections can become quite crowded. (2) If the objects leave the field of view, no velocities can be measured. (3) If the objects move in an unsteady way, the obtained velocity values can be of questionable significance because the obtained velocities are average values over a certain time/distance.

2. Kymographs

Kymographs are space–time plots which display intensity values along a predefined path over time. Thus, in contrast to maximum projections, they can resolve time information. The cost is spatial information, which is reduced by projection from 2D to 1D. In order to measure velocities based upon kymographs, the path of the moving object has to be marked. A function within the data-processing software then generates the kymograph. Depending on the software either a direct measurement of velocities is possible or the lengths along the time and space axis have to be measured in order to calculate the velocities. While more labor intensive to generate, kymographs exhibit the major advantage of displaying the actual velocity (given by the slope of the kymograph) at a certain point in time or space (Fig. 2F and G).

B. Nanometer Tracking in Two Dimensions

Fluorescent objects with a size much smaller than the wavelength of light (and/or of known geometry) can be localized with much higher precision than the resolution of an optical microscope (usually about 200 nm for visible light) (Anderson *et al.*, 1992; Gelles *et al.*, 1988; Hua *et al.*, 1997; Yildiz *et al.*, 2003). We will describe a method to determine the position of single particles (QDs) and filaments (microtubules) using Gaussian-function-based models.

1. Tracking of Quantum Dots

QDs with a diameter of $\approx$20 nm appear as point sources of light; therefore, their intensity profile can be regarded identical to the Point-Spread-Function (PSF) of the imaging system. The PSF is well approximated by a 2D-Gaussian function (Cheezum *et al.*, 2001; Thompson *et al.*, 2002), and the localization of fluorescent particles by fitting the intensity profile to this model has become standard. When implementing this approach, one possibility is to fit intensity profiles of fluorescent particles to radially symmetric 2D-Gaussian functions with a fixed width corresponding to the dimension of the PSF [Eq. (1), σ fixed]. However, we found it important to also allow radially symmetric 2D-Gaussian functions with non-fixed widths [Eq. (1), σ not fixed] as well as elliptical 2D-Gaussian functions [Eq. (2) representing the probability density function of a bivariate normal distribution (Hogg and Craig, 1978)]. By allowing these additional degrees of freedom, fitting can accommodate slightly defocused images as well as particles with sizes large enough to increase the widths of their images beyond the width of the PSF (such as fluorescent beads in the 100-nm range). As a consequence, our fitting can readily be used to calculate precise intensity values corresponding to

the volumes under the 2D-Gaussian functions [e.g., for FLIC-based height measurements (see Section III.C)].

$$I(x,y) = \frac{h}{2\pi\sigma^2} \cdot \exp\left[-\frac{(x-\hat{x})^2 + (y-\hat{y})^2}{2\sigma^2}\right] \tag{1}$$

$$I(x,y) = \frac{h}{2\pi\sigma_x\sigma_y\sqrt{1-\rho^2}} \cdot \exp \times \left[-\frac{1}{(1-\rho^2)}\left(\frac{(x-\hat{x})^2}{2\sigma_x^2} - \rho\frac{(x-\hat{x})}{\sigma_x}\frac{(y-\hat{y})}{\sigma_y} + \frac{(y-\hat{y})^2}{2\sigma_y^2}\right)\right] \tag{2}$$

Here *I(x,y)* denotes the value of the 2D-Gaussian function at position *x, y; h* denotes the height of the Gaussian function; $\hat{x}$, $\hat{y}$ denote the position of the center of the fitting function; for Eq. (1) σ denotes the width of the symmetric 2D-Gaussian function; for Eq. (2) σ_x, σ_y denote the widths of the elliptical Gaussian function in *x–y* directions (however, *x–y* directions are not generally coinciding with the two axes of the ellipse); and ρ denotes a correlation coefficient influencing orientation and shape of the Gaussian function—these parameters can be converted to (1) the actual widths of the Gaussian function along the major and minor axis of the ellipse and (2) to the angle between the major axis of the ellipse and the *x*-axis.

Using the described tracking approach for microtubule-attached QDs, we were able to resolve the 8-nm steps (see Fig. 3B) that kinesin-1 takes on the microtubule lattice, and even 4-nm steps of microtubules, which occur when microtubules are driven by two kinesin-1 motors in a gliding motility assay (Leduc *et al.*, 2007). In these experiments, we used the specific advantages of the gliding assay to count the number of (processive) motors acting on the microtubule. First, the GFP-labeled motors were well separated and could be identified as single molecules being colocalized with microtubules. Second, the microtubule itself indicated the number of motors involved in transport at very low motor density: the microtubule swiveled if only one motor was interacting with it. The transition to a nonswiveling state then corresponded to the case of two active motors.

2. Tracking of Microtubules

Compared to fluorescent objects with subresolution size in all dimensions, microtubules (densely labeled with fluorophores) create a much more complex intensity profile. Although subresolution-sized in their diameter, microtubules have a typical length of several microns. It is therefore practically impossible to fit the entire microtubule shape using a single fitting function. To tackle this problem, we have developed an algorithm that separates the filament into segments (see Fig. 4). The intensity profiles of the segments are then fitted to appropriate model functions (see Fig. 3A). The positions and orientations of the segments are finally combined and the contour of the microtubule is interpolated to create a continuous line between two end points. It has to be noted that the segments that include the microtubule ends have to be fitted to a different Gaussian-function-based model than the inner segments of the filament.

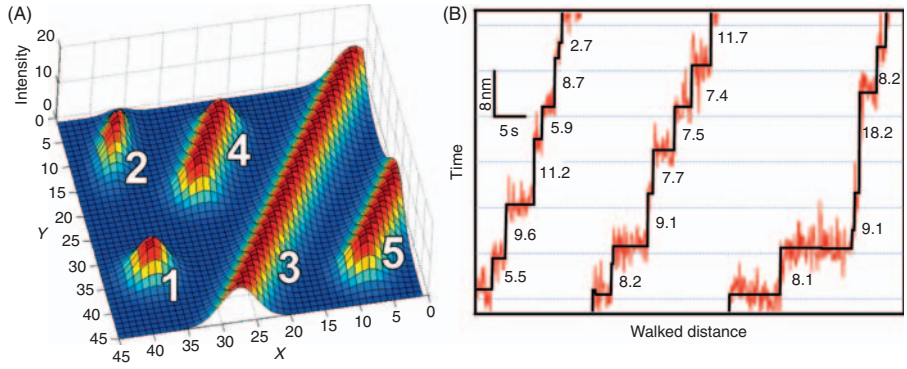

Fig. 3 Principle and application of 2D-tracking based on fitting intensity profiles to 2D-Gaussian models. (A) Intensity profiles of the models used to fit microtubule segments: (1) symmetric 2D-Gaussian function, (2) stretched 2D-Gaussian function, (3) short filament, (4) filament ridge, (5) end segment of filament. (B) 8-nm steps corresponding to the operation of a single kinesin-1 molecule on a microtubule. (See Plate no. 18 in the Color Plate Section.)

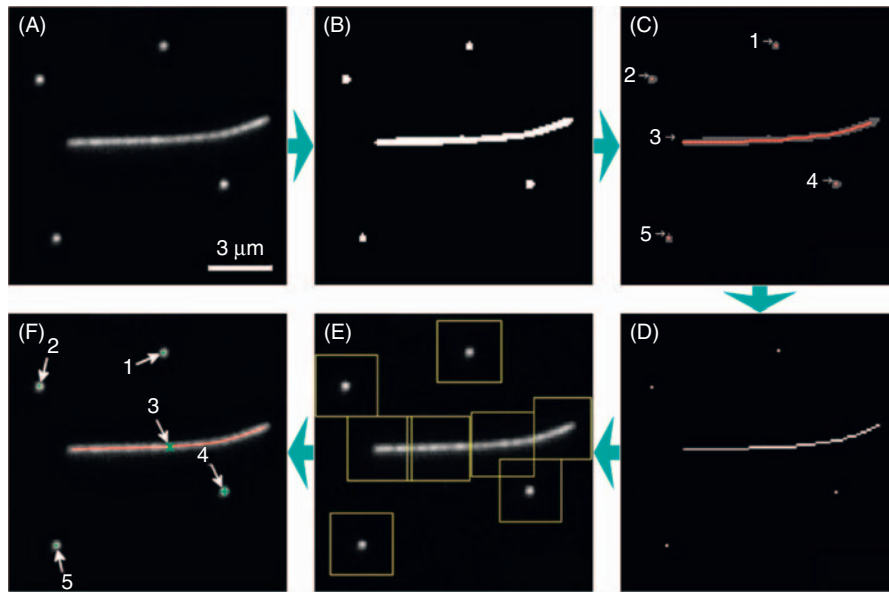

Fig. 4 General approach for tracking within a single frame. The grayscale image (A) is converted to a binary image (B) using an intensity threshold value. Objects are classified into particles (1, 2, 4, 5) and filaments (3) (C). A thinning algorithm (Lam *et al.*, 1992) is applied to calculate the skeleton of the image (D). The skeleton features are used to assign regions and appropriate fitting models to the particles and filament segments (E). Using estimated starting parameters, the regions are fitted separately, and for the filaments, the results are interpolated. The final tracking data are displayed in a graphical user interface: particle center (+), filament center (×), and filament contour (red line) (F). (See Plate no. 19 in the Color Plate Section.)

Tip: Microtubules can also be localized using 1D-Gaussian functions perpendicular to their longitudinal axis. However, we found that the orientation of the filaments had a high impact on the precision, which is not the case using the algorithm described above.

3. Implementation of the Tracking Routines

Our MatLab (The MathWorks, Natick, MA) based tracking algorithm (Ruhnow, in preparation) is designed to analyze large sets of data. The implementation is therefore entirely automated, however, still keeping the possibility to optionally adjust various parameters. In a first step, every frame is processed individually to determine the positions of all objects (see Fig. 4): (1) *Rough scanning:* Grayscale images are converted to binary images using predefined threshold values. Objects with intensity values above this threshold are classified as particles or filaments according to their area and shape. After applying a thinning algorithm (Lam *et al.*, 1992), different fitting regions and fitting models (according to Fig. 3) are assigned to the individual particles and filament segments. (2) *Fine scanning:* The regions are fitted with estimated starting parameters. The algorithm employs a nonlinear least-squares fitting routine (Coleman and Li, 1994; Moré, 1977) and estimates the error for each parameter. Overlaying regions (e.g., crossing microtubules) are combined and fitted using the sum of their initial models. (3) *Interpolating filament shape:* The contour between the two end points of a filament is derived using a spline interpolation based on the x–y positions and the orientation of the fitted filament segments.

In a second step, the fitted particle and filament positions from individual frames are connected into tracks using an adapted feature point tracking algorithm (Chetverikov and Verestóy, 1999). Thereby, a cost function for four subsequent frames is calculated and includes parameters like position, velocity, direction, intensity, or length. Particles and filaments, albeit processed simultaneously, are connected in separate tracks to preclude interference. Occlusions are handled with a post-processing step, where corresponding tracks are merged automatically. The final tracking results can be displayed in an overlay with the original images offering manual verification of the fitting. Tracks can be edited, merged, and analyzed using additional customized tools, including the possibility to relate the positions of the particles to the contours of the microtubules (Nitzsche *et al.*, 2008).

Precise tracking of the microtubules also provides an effective tool to determine the number of transporting motors at low to intermediate motor densities. The microtubules will be "pinpointed" by the active motors, resulting in reduced sideways fluctuations of the microtubule at the motor positions.

C. Resolving Nanometer Distances in the Third Dimension

When applying 2D-nanometer tracking to study the interaction of motor proteins with microtubules, the achieved understanding will always remain incomplete, because the molecules operate in 3D space. To complement 2D microscopic results with data from the third dimension, a number of approaches based on dual-focus imaging (Toprak *et al.*, 2007; Watanabe *et al.*, 2007) or split-image methods (Sun *et al.*, 2009; Yajima *et al.*, 2008) have recently been proposed and demonstrated. While these approaches are well capable of providing nanometer accuracy in the third dimension, they are technically demanding and require sophisticated microscope setups. In the following, we will describe an alternative, simple-to-implement, approach based on FLIC microscopy (Kerssemakers *et al.*, 2006; Lambacher and Fromherz, 1996), which relies on interference effects of excitation and emission light within a distance of about 1 μm from a reflecting surface. We will demonstrate this

method on the examples to measure the absolute height of gliding microtubules above the substrate surface (corresponding to the cargo-microtubule distance during active transport) and to observe rotations of gliding microtubules around their longitudinal axis (corresponding to helical paths of the motor proteins on the microtubule surface).

1. Measuring the Heights of Gliding Microtubules

The experimental setup to measure the heights of gliding, fluorescently labeled microtubules above a reflective surface is schematically depicted in Fig. 5. Interference effects lead to a vertical modulation of the detected emission intensity, which can be calibrated using tilted microtubules as nanoscopic rulers. When immobilized under a fixed tilt angle in a low concentration agarose gel, these microtubules exhibit a zebra-stripe intensity modulation when imaged on the camera chip (i.e., in the x–y plane). A side view onto the microtubules (obtained by z-plane sectioning) provides the tilt angle and allows for the precise determination of the FLIC curve. The height of moving microtubules can then be obtained by mapping their intensity onto the FLIC curve (Kerssemakers *et al.*, 2006).

Alternatively, an independent method to determine the height of gliding microtubules above a surface relies on thermally oxidized Si-wafers into which nonoverlapping patches (sizes approximately $10 \times 10\,\mu m$) of different depths are etched [similar to Lambacher and Fromherz (1996)]. Microtubules moving over the SiO_2 steps will change their distance above the reflecting Si/SiO_2 interface and thus their intensity. Ratios of background-corrected fluorescence intensity values can then be obtained for each SiO_2 step. Because local intensity ratios—instead of absolute intensities—are derived here, the values are independent of spatial inhomogeneities in the illumination. The obtained data points for gliding microtubules as well as microtubules that are immobilized directly on the surface can be well fit by modified

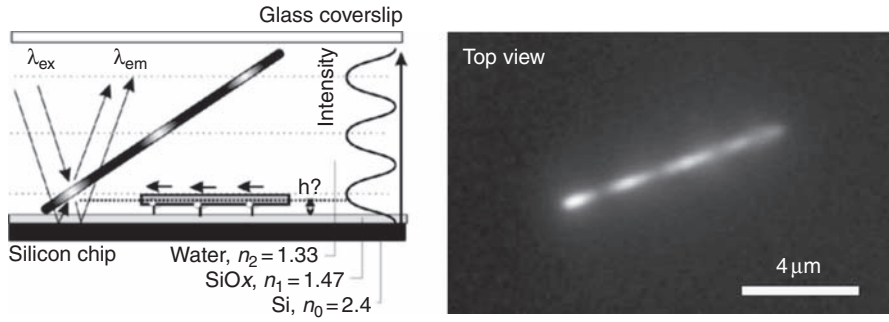

Fig. 5 Principle of quantitative FLIC microscopy on microtubules. Fluorescent, tilted microtubules close to a reflecting silicon surface (upon which a thin layer of silicon oxide has been thermally grown) are used as nanoscopic calibration rulers. Light with wavelength λ_{ex} may either excite the fluorophores in the microtubules directly or via the reflecting Si/SiO_2 interface. A similar light path exists for the light emitted by the fluorophores (λ_{em}). Thereby, the microtubules are illuminated and imaged from the glass side of a microscopic flow chamber in aqueous buffer. The height of moving microtubules can be obtained by mapping their intensity onto that of a fixed, tilted microtubule (left). Fluorescent image of a tilted microtubule as captured on the CCD camera chip (right).

FLIC curves. The lateral shift in the peaks of these curves then corresponds to the height difference between motile and surface-immobilized microtubules (Kerssemakers *et al.*, 2006).

2. Measuring Height Changes of Quantum Dots

When a fluorescent probe is being imaged by FLIC microscopy, the recorded intensity of the probe directly represents a measure of its height above the reflective surface. While it is difficult to judge the absolute height of such objects from individual images, changes in height (over time) can be easily visualized. Both maximum projections (Fig. 6A) and kymographs of FLIC movies provide a direct visual representation for the movement of mobile objects with nanometer sensitivity in the *z*-direction.

If nanometer sensitivity in all three dimensions is desired, the intensity information of the QDs (Fig. 6B) can be combined with the results from 2D-nanometer tracking. This way, we were able to characterize the pitch and orientation of the axial motion of microtubules in gliding assays (Nitzsche *et al.*, 2008).

IV. Future Directions

Studying the interactions of motor proteins with microtubules will continue to be an exciting field of biophysical research. In particular, investigations on cooperative motor effects will come more and more into focus. Gliding motility assays will be of great use in this research especially (1) when nonprocessive motors are to be investigated, (2) when the exact number of engaged motors needs to be known, (3) when microtubules are driven by a large number of motors (e.g., to study forces in motility systems using optical or magnetic tweezers), and (4) when motors of different directionality are to be combined on structured or unstructured motor surfaces. Moreover, gliding motility assays constitute the main framework for nanotechnological applications of biomolecular motors (Goel and Vogel, 2008; Hess and Vogel, 2001; van den Heuvel and Dekker, 2007). Reliable motility assays need to be developed for various synthetic environments. The described tracking

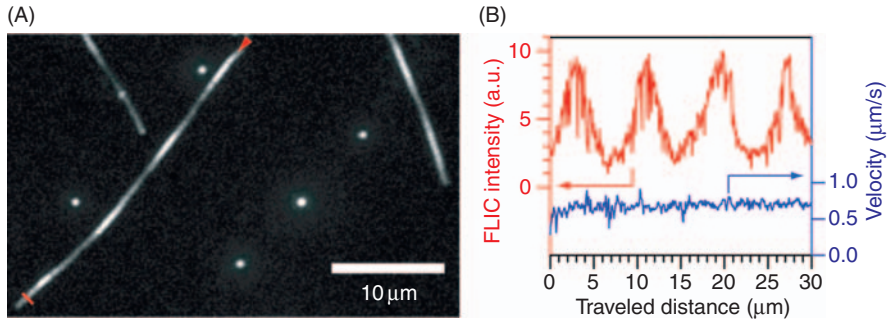

Fig. 6 Analyzing the axial rotation of gliding microtubules by following the up and down motion of the attached QDs. (A) Maximum projection of QD signal acquired at 10 frames per second. (B) FLIC intensity versus traveled distance of the QD obtained by nanometer tracking. Data correspond to part of the maximum projection marked by the red arrow and bar in (A). (See Plate no. 20 in the Color Plate Section.)

algorithms are readily applicable to molecular detection systems in which the velocity of gliding microtubules is used as readout parameter (Korten and Diez, 2008), or to novel surface imaging methods in which the intensity values of gliding microtubules can be used to probe nanometer-sized topographical surface features (Kerssemakers *et al.*, 2009). Similarly, the developed filament tracking routines will be of benefit in microtubule–microtubule sliding (Fink *et al.*, 2009) and depolymerization assays (Helenius *et al.*, 2006; Varga *et al.*, 2009).

Regarding the tracking precision, nanometer accuracy at an acquisition rate of 10 frames per second is easily possible with the described methods. However, when aiming for significantly faster imaging, the tracking precision is compromised with currently available probes. We therefore expect that the development of novel bright, nonblinking fluorescent probes as well as highly-scattering metal nanoparticles—all very well attachable to gliding microtubules—will contribute greatly to further improve the optical 3D-nanometry approaches.

Acknowledgments

The authors would like to thank all current and former members of the Howard and Diez laboratories for their tremendous efforts in helping to develop the described protocols. In addition, we thank Franziska Friedrich for the illustration of Fig. 1 as well as Marcus Braun and Gero Fink for valuable comments on the manuscript.

Reagents

- Alexa Fluor 488 5-TFP (Invitrogen Corporation, Carlsbad, CA, USA, #A30005).
- ATP (Roche Diagnostics GmbH, Mannheim, Germany, #10519979001).
- BME, β-mercaptoethanol (Sigma-Aldrich, St. Louis, MO, USA, #M6250); BME is kept in glass vials at 4°C for up to 1 month.
- BRB80 (80 mM PIPES, pH 6.9, with KOH, 1 mM EGTA, 1 mM $MgCl_2$).
- Casein (Sigma-Aldrich, St. Louis, MO, USA, #C7078); add 35 ml BRB80 to 1 g casein in a 50-ml centrifuge tube (e.g., Corning Inc., Corning, NY, USA, #430829). Place the Falcon tube in a rotating wheel at 4°C and allow the casein to dissolve overnight. Let the large precipitates sediment in the Falcon tube placed upright. Centrifuge the supernatant at 10,000 × *g* at 4°C for 5 min. Filter the supernatant using a 0.2-μm syringe filter. After adjusting the concentration to the desired value (e.g., 10 mg/ml), snap-freeze 40 μl aliquots in liquid nitrogen, and store at –20°C.
- Catalase (Sigma-Aldrich, St. Louis, MO, USA, #C9322); stock solution is made at 2 mg/ml in BRB80, 10 μl aliquots are snap-frozen in liquid nitrogen, and stored at –20°C.
- Chloroform (VWR International, West Chester, PA, USA, #1.02444).
- D-glucose (Sigma-Aldrich, St. Louis, MO, USA, #G-7528); stock solution is made at 2 M in water, 10 μl aliquots are stored at –20°C.
- DTT, 1,4-Dithio-DL-threitol (Sigma-Aldrich, St. Louis, MO, USA, #43815); stock solution: 1 M in nanopure water, stored at –20°C.
- EGTA, ethylene glycol tetraacetic acid (Sigma-Aldrich, St. Louis, MO, USA, #E4378).

- Ethanol (VWR International, West Chester, PA, USA, #1.00983.2511).
- Glass coverslips (Corning Incorporated Life Sciences, Lowell, MA, USA, #2870-22 or #2870-18).
- Glucose oxidase (SERVA Electrophoresis GmbH, Heidelberg, Germany, #22778); stock solution is made at 20 mg/ml in BRB80; 10 µl aliquots are snap-frozen in liquid nitrogen, and stored at –20°C.
- GMP-CPP (Jena Bioscience GmbH, Jena, Germany, #NU-405L).
- HCl (37%, Merck KGaA, Darmstadt, Germany, #100317).
- Hydrogen peroxide 30% (Sigma-Aldrich, St. Louis, MO, USA, #21.676-3).
- Kinesin-1; we use full-length *Drosophila* kinesin-1 that is purified by applying published protocols (Hancock and Howard, 1998).
- KOH-pellets (Merck KGaA, Darmstadt, Germany, #1.05012).
- $MgCl_2$ (VWR International, West Chester, PA, USA, #1.05833).
- Mucasol (VWR International, West Chester, PA, USA, #148-1111).
- Nescofilm (Carl Roth GmbH & Co. KG, Karlsruhe, Germany, #2569.1).
- Parafilm M (Pechiney Plastic Packaging, Menasha, WI, USA).
- PEG-NH_2 ($M_n = 5000$ g/mol, $M_w = 5400$ g/mol; Polymer Source Inc., Dorval, Quebec, Canada, #P2161-EGOCH3NH2).
- PEG-silane, 2-[Methoxy(polyethyleneoxy)propyl]trimethoxysilane [90% (ABCR GmbH & Co. KG, Karlsruhe, Germany, #AB111226, CAS 65994-07-2)].
- Penta-His antibodies (Qiagen Inc., Valencia, CA, USA, #34660).
- PGMA, Polyglycidylmethacrylate ($M_n = 50{,}000$ g/mol) was synthesized by free radical polymerization of glycidyl methacrylate (Sigma-Aldrich, St. Louis, MO, USA, #64161) as described previously (Ionov *et al.*, 2005).
- PIPES (Sigma-Aldrich, St. Louis, MO, USA, #80635).
- Pluronic F127 (Sigma-Aldrich, St. Louis, MO, USA, #P2443) stock solution is made at 1% in BRB80, filtered using a 0.2-µm syringe filter, and stored at 4°C.
- Qdots 655 (Invitrogen Corporation, Carlsbad, CA, USA, #Q10121MP).
- Sigillum Wax (Servoprax GmbH, Wesel, Germany, #A1 0303).
- Silicon wafer chips (50×10 mm, {100} orientation; Semiconductor Processing Co, Boston, MA, USA or 10×10 mm with oxide layers of ≈30 nm, GESIM, Großerkmannsdorf, Germany).
- Sulfuric acid (Merck KGaA, Darmstadt, Germany, #1.00732.2500).
- TAMRA (Invitrogen Corporation, Carlsbad, CA, USA, #C1171).
- Taxol (Paclitaxel; Sigma-Aldrich, St. Louis, MO, USA, #T7191).
- Tetraspeck fluorescent microspheres (0.2 µm, #T7280, Invitrogen Corporation, Carlsbad, CA, USA).
- Toluene (Sigma-Aldrich, St. Louis, MO, USA, #34929).
- Tubulin, bovine (Cytoskeleton Inc., Denver, CO, USA; biotinylated #5.11.2147; unlabeled #5.11.2146; rhodamine labeled #5.11.2148).
- Tubulin, pig [tubulin is purified from pig brain as described in (Hunter *et al.*, 2003) and labeled (e.g., with TAMRA or Alexa Fluor 488) as described in Hyman *et al.* (1991)].
- Vacuum grease (High vacuum grease, Dow Corning Corporation, Midland, MI, USA).
- Water, nanopure ($>18\ M\Omega m^{-1}$).

References

Anderson, C. M., Georgiou, G. N., Morrison, I. E., Stevenson, G. V., and Cherry, R. J. (1992). Tracking of cell surface receptors by fluorescence digital imaging microscopy using a charge-coupled device camera. Low-density lipoprotein and influenza virus receptor mobility at 4 degrees C. *J. Cell Sci.* **101** (Pt 2), 415–425.

Bieling, P., Laan, L., Schek, H., Munteanu, E. L., Sandblad, L., Dogterom, M., Brunner, D., and Surrey, T. (2007). Reconstitution of a microtubule plus-end tracking system in vitro. *Nature* **450**(7172), 1100–1105.

Bieling, P., Telley, I. A., Piehler, J., and Surrey, T. (2008). Processive kinesins require loose mechanical coupling for efficient collective motility. *Embo Rep.* **9**(11), 1121–1127.

Brouhard, G. J., Stear, J. H., Noetzel, T. L., Al-Bassam, J., Kinoshita, K., Harrison, S. C., Howard, J., and Hyman, A. A. (2008). XMAP215 is a processive microtubule polymerase. *Cell* **132**(1), 79–88.

Caplow, M., Ruhlen, R. L., and Shanks, J. (1994). The free-energy for hydrolysis of a microtubule-bound nucleotide triphosphate is near zero – all of the free-energy for hydrolysis is stored in the microtubule lattice. *J. Cell Biol.* **127**(3), 779–788.

Caplow, M., and Shanks, J. (1996). Evidence that a single monolayer tubulin-GTP cap is both necessary and sufficient to stabilize microtubules. *Mol. Biol. Cell.* **7**(4), 663–675.

Cheezum, M. K., Walker, W. F., and Guilford, W. H. (2001). Quantitative comparison of algorithms for tracking single fluorescent particles. *Biophys. J.* **81**(4), 2378–2388.

Chen, Y., Vela, J., Htoon, H., Casson, J. L., Werder, D. J., Bussian, D. A., Klimov, V. I., and Hollingsworth, J. A. (2008). "Giant" multishell CdSe nanocrystal quantum dots with suppressed blinking. *J. Am. Chem. Soc.* **130**(15), 5026–.

Chetverikov, D., and Verestóy, J. (1999). Feature point tracking for incomplete trajectories. *Computing* **62**(4),321–338.

Coleman, T. F., and Li, Y. (1994). On the convergence of reflective newton methods for large-scale nonlinear minimization subject to bounds. *Math. Program* **67**(2), 189–224.

Crevenna, A. H., Madathil, S., Cohen, D. N., Wagenbach, M., Fahmy, K., and Howard, J. (2008). Secondary structure and compliance of a predicted flexible domain in Kinesin-1 necessary for cooperation of motors. *Biophys. J.* **95**(11), 5216–5227.

deCastro, M. J., Ho, C. H., and Stewart, R. J. (1999). Motility of dimeric ncd on a metal-chelating surfactant: Evidence that ncd is not processive. *Biochemistry* **38**(16), 5076–5081.

Fink, G., Hajdo, L., Skowronek, K.J., Reuther, C., Kasprzak, A. A., and Diez, S. (2009). The mitotic kinesin-14 Ncd drives directional microtubule-microtubule sliding. *Nat. Cell Biol.* **11**(6), 717–U747.

Funatsu, T., Harada, Y., Tokunaga, M., Saito, K., and Yanagida, T. (1995). Imaging of single fluorescent molecules and individual atp turnovers by single myosin molecules in aqueous-solution. *Nature* **374** (6522), 555–559.

Gelles, J., Schnapp, B. J., and Sheetz, M. P. (1988). Tracking kinesin-driven movements with nanometre-scale precision. *Nature* **331**(6155), 450–453.

Giepmans, B. N.G., Adams, S. R., Ellisman, M. H., and Tsien, R. Y. (2006). Review – The fluorescent toolbox for assessing protein location and function. *Science* **312**(5771), 217–224.

Goel, A., and Vogel, V. (2008). Harnessing biological motors to engineer systems for nanoscale transport and assembly. *Nat. Nanotechnol.* **3**(8), 465–475.

Hancock, W. O., and Howard, J. (1998). Processivity of the motor protein kinesin requires two heads. *J. Cell Biol.* **140**(6), 1395–1405.

Helenius, J., Brouhard, G., Kalaidzidis, Y., Diez, S., and Howard, J. (2006). The depolymerizing kinesin MCAK uses lattice diffusion to rapidly target microtubule ends. *Nature* **441**(7089), 115–119.

Hess, H., and Vogel, V. (2001). Molecular shuttles based on motor proteins: Active transport in synthetic environments. *J. Biotechnol.* **82**(1), 67–85.

Hogg, R. V., and Craig, A. T. (1978). "Introduction to Mathematical Statistics." 4th edn. Macmillan Publishing Co., Inc, New York.

Hohng, S., and Ha, T. (2004). Near-complete suppression of quantum dot blinking in ambient conditions. *J. Am. Chem. Soc.* **126**(5), 1324–1325.

Howard, J., Hudspeth, A. J., and Vale, R. D. (1989). Movement of microtubules by single kinesin molecules. *Nature* **342**(6246), 154–158.

Howard, J., Hunt, A., and Baek, S. (1993). Assay of microtubule movement driven by single kinesin molecules. *Meth. Cell Biol.* **39**, 137–147.

Hua, W., Young, E. C., Fleming, M. L., and Gelles, J. (1997). Coupling of kinesin steps to ATP hydrolysis. *Nature* **388**(6640), 390–393.

Hunter, A. W., Caplow, M., Coy, D. L., Hancock, W. O., Diez, S., Wordeman, L., and Howard, J. (2003). The kinesin-related protein MCAK is a microtubule depolymerase that forms an ATP-hydrolyzing complex at microtubule ends. *Mol. Cell* **11**(2), 445–457.

Hyman, A. A., Chretien, D., Arnal, I., and Wade, R. H. (1995). Structural changes accompanying GTP hydrolysis in microtubules: Information from a slowly hydrolyzable analogue guanylyl-(alpha,beta)-methylene-diphosphonate. *J. Cell Biol.* **128**(1-2), 117–125.

Hyman, A., Drechsel, D., Kellogg, D., Salser, S., Sawin, K., Steffen, P., Wordeman, L., and Mitchison, T. (1991). Preparation of modified tubulins. *Meth. Enzymol.* **196**, 478–485.

Ionov, L., Stamm, M., and Diez, S. (2005). Size sorting of protein assemblies using polymeric gradient surfaces. *Nano Lett.* **5**(10), 1910–1914.

Kerssemakers, J., Howard, J., Hess, H., and Diez, S. (2006). The distance that kinesin-1 holds its cargo from the microtubule surface measured by fluorescence interference contrast microscopy. *Proc. Natl. Acad. Sci. U.S.A.* **103**(43), 15812–15817.

Kerssemakers, J., Ionov, L., Queitsch, U., Luna, S., Hess, H., and Diez, S. (2009). 3D nanometer tracking of motile microtubules on reflective surfaces. *Small* **5**(15), 1732–1737.

Korten, T. (2009). "How Kinesin-1 Deals with Roadblocks: Biophysical Description and Nanotechnological Application". Doctoral dissertation, TU Dresden, urn:nbn:de:bsz:14-qucosa-26443.

Korten, T., and Diez, S. (2008). Setting up roadblocks for kinesin-1: Mechanism for the selective speed control of cargo carrying microtubules. *Lab Chip* **8**(9), 1441–1447.

Kron, S. J., and Spudich, Ja. (1986). Fluorescent actin-filaments move on myosin fixed to a glass-surface. *Proc. Natl. Acad. Sci. U.S.A.* **83**(17), 6272–6276.

Lam, L., Lee, S. -W., and Suen, C. Y. (1992). Thinning methodologies – A comprehensive survey. *IEEE Trans. Pattern Anal. Mach. Intell.* **14**(9), 879.

Lambacher, A., and Fromherz, P. (1996). Fluorescence interference-contrast microscopy on oxidized silicon using a monomolecular dye layer. *Appl. Phys. A Mater. Sci. Process.* **63**(3), 207–216.

Leduc, C., Ruhnow, F., Howard, J., and Diez, S. (2007). Detection of fractional steps in cargo movement by the collective operation of kinesin-1 motors. *Proc. Natl. Acad. Sci. U.S.A.* **104**(26), 10847–10852.

Mahler, B., Spinicelli, P., Buil, S., Quelin, X., Hermier, J. P., and Dubertret, B. (2008). Towards non-blinking colloidal quantum dots. *Nat. Mater.* **7**(8), 659–664.

Meurer-Grob, P., Kasparian, J., and Wade, R. H. (2001). Microtubule structure at improved resolution. *Biochemistry* **40**(27), 8000–8008.

Moré, J. J. (1977). The Levenberg-Marquardt algorithm: Implementation and theory. In *"Numerical Analysis"* (Watson G. A. ed.), **Vol. Lecture Notes in Mathematics 630**, pp. 105–116. Springer, Berlin.

Nagashima, H., and Asakura, S. (1980). Dark-field light microscopic study of the flexibility of F-Actin complexes. *J. Mol. Biol.* **136**(2), 169–182.

Nitzsche, B., Ruhnow, F., and Diez, S. (2008). Quantum-dot-assisted characterization of microtubule rotations during cargo transport. *Nat. Nanotechnol.* **3**(9), 552–556.

Ozeki, T., Verma, V., Uppalapati, M., Suzuki, Y., Nakamura, M., Catchmark, J. M., and Hancock, W. O. (2009). Surface-bound casein modulates the adsorption and activity of kinesin on SiO_2 surfaces. *Biophys. J.* **96**(8), 3305–3318.

Papra, A., Gadegaard, N., and Larsen, N. B. (2001). Characterization of ultrathin poly(ethylene glycol) monolayers on silicon substrates. *Langmuir.* **17**(5), 1457–1460.

Pierce, D. W., HomBooher, N., and Vale, R. D. (1997). Imaging individual green fluorescent proteins. *Nature* **388**(6640), 338–338.

Pierson, G. B., Burton, P. R., and Himes, R. H. (1978). Alterations in number of protofilaments in microtubules assembled in vitro. *J. Cell Biol.* **76**(1), 223–228.

Ray, S., Meyhofer, E., Milligan, R. A., and Howard, J. (1993). Kinesin follows the microtubule's protofilament axis. *J. Cell Biol.* **121**(5), 1083–1093.

Resch-Genger, U., Grabolle, M., Cavaliere-Jaricot, S., Nitschke, R., and Nann, T. (2008). Quantum dots versus organic dyes as fluorescent labels. *Nat. Methods* **5**(9), 763–775.

Rief, M., Rock, R. S., Mehta, A. D., Mooseker, M. S., Cheney, R. E., and Spudich, J. A. (2000). Myosin-V stepping kinetics: A molecular model for processivity. *Proc. Natl. Acad. Sci. U.S.A.* **97**(17), 9482–9486.

Ruhnow, F. (in preparation).

Schnitzer, M. J., Visscher, K., and Block, S. M. (2000). Force production by single kinesin motors. *Nat. Cell Biol.* **2**(10), 718–723.

Sheetz, M. P., and Spudich, Ja. (1983). Movement of myosin-coated fluorescent beads on actin cables in vitro. *Nature* **303**(5912), 31–35.

Spudich, J. A., Kron, S. J., and Sheetz, M. P. (1985). Movement of myosin-coated beads on oriented filaments reconstituted from purified actin. *Nature* **315**(6020), 584–586.

Sun, Y., McKenna, J. D., Murray, J. M., Ostap, E. M., and Goldman, Y. E. (2009). Parallax: High accuracy three-dimensional single molecule tracking using split images. *Nano Lett.* **9**(7), 2676–2682.

Svoboda, K., Schmidt, C. F., Schnapp, B. J., and Block, S. M. (1993). Direct observation of kinesin stepping by optical trapping interferometry. *Nature* **365**(6448), 721–727.

Thompson, R. E., Larson, D. R., and Webb, W. W. (2002). Precise nanometer localization analysis for individual fluorescent probes. *Biophys. J.* **82**(5), 2775–2783.

Toprak, E., Balci, H., Blehm, B. H., and Selvin, P. R. (2007). Three-dimensional particle tracking via bifocal imaging. *Nano Lett.* **7**(7), 2043–2045.

Vale, R. D., Funatsu, T., Pierce, D. W., Romberg, L., Harada, Y., and Yanagida, T. (1996). Direct observation of single kinesin molecules moving along microtubules. *Nature* **380**(6573), 451–453.

van den Heuvel, M. G., and Dekker, C. (2007). Motor proteins at work for nanotechnology. *Science* **317**(5836), 333–336.

Varga, V., Helenius, J., Tanaka, K., Hyman, A. A., Tanaka, T. U., and Howard, J. (2006). Yeast kinesin-8 depolymerizes microtubules in a length-dependent manner. *Nat. Cell Biol.* **8**(9), 957–960.

Varga, V., Leduc, C., Bormuth, V., Diez, S., and Howard, J. (2009). Kinesin-8 motors act cooperatively to mediate length-dependent microtubule depolymerization. *Cell* **138**(6), 1174–1183.

Wang, X. Y., Ren, X. F., Kahen, K., Hahn, M. A., Rajeswaran, M., Maccagnano-Zacher, S., Silcox, J., Cragg, G. E., Efros, A. L., and Krauss, T. D. (2009). Non-blinking semiconductor nanocrystals. *Nature* **459**(7247), 686–689.

Watanabe, T. M., Sato, T., Gonda, K., and Higuchi, H. (2007). Three-dimensional nanometry of vesicle transport in living cells using dual-focus imaging optics. *Biochem. Biophys. Res. Commun.* **359**(1), 1–7.

Yajima, J., Mizutani, K., and Nishizaka, T. (2008). A torque component present in mitotic kinesin Eg5 revealed by three-dimensional tracking. *Nat. Struct. Mol. Biol.* **15**(10), 1119–1121.

Yanagida, T., Nakase, M., Nishiyama, K., and Oosawa, F. (1984). Direct observation of motion of single F-Actin filaments in the presence of myosin. *Nature* **307**(5946), 58–60.

Yildiz, A., Forkey, J. N., McKinney, S. A., Ha, T., Goldman, Y. E., and Selvin, P. R. (2003). Myosin V walks hand-over-hand: Single fluorophore imaging with 1.5-nm localization. *Science* **300**(5628), 2061–2065.